Comprehensive Study of Sub-grain Boundaries in Si Bulk Multicrystals

A new approach, combination of defects characterization technique using x-ray diffraction and model crystal growth experiments, was applied to investigate the physics of Si bulk multicrystals. This provides fundamental knowledge of sub-grain boundaries, which is of crucial importance to improve crystal quality of Si bulk multicrystals applicable to high efficiency solar cells.

Over the past decade, Si bulk multicrystal has emerged as the substrate material for commercial solar cells. To accelerate the adoption of solar cells to the world, ongoing research targets further reductions in energy costs by improving material performance, while reducing manufacturing costs and raw material costs. We approached this issue from deep understanding of crystal physics of Si multicrystals, namely formation mechanism of multicrystalline structure and generation mechanism and properties of defects. The former study lead us to proposal of the dendritic casting method [1]. This article presents the latter study.

Among the defects in the Si bulk multicrystals, we focused on sub-grain boundaries (sub-GBs) because they are known to perform as serious carrier recombination sites for solar cells. To improve the crystal quality of Si multicrystals, we must comprehensively clarify the physics of sub-GBs, i.e. 1) electrical properties, 2) interaction with impurities and strain, 3) generation, propagation and vanishing mechanisms and 4) influence of grain boundary structure and crystal orientations, as illustrated in Fig.1.

We firstly applied spatially-resolved x-ray diffraction to defects characterization of Si bulk multicrystals to precisely analyze structure and distribution of sub-GBs. Coordinating their high angular resolution with crystallographic multicrystalline structure, we succeeded in detecting the sub-GBs with small angle difference, as shown in Fig.2. We found that sub-GBs distribute locally and tend to propagate to the growth direction of the ingot across some grain boundaries. Following the structural characterization, we revealed their electrical properties they are significantly electrically active and work as current leakage sites for solar cells. This fundamental
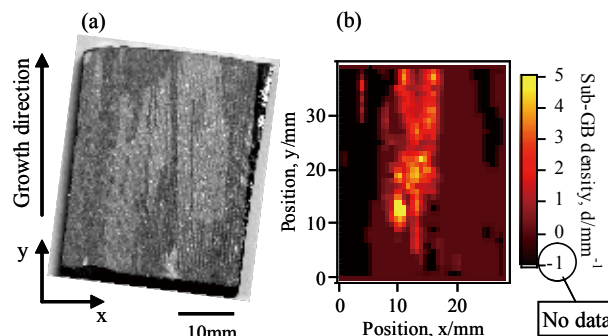

Fig.2. (a) Cross-section of the sample, (b) distribution of sub-GBs density analyzed by spatially-resolved x-ray diffraction.

study gave common recognition of sub-GBs as dominant defects of the solar cells.

Although we were able to investigate structure, distribution and electrical properties of sub-GBs in the practical growth method, it is difficult to clarify the generation mechanisms due to the random and complicated multicrystalline structures. We therefore developed model crystal growth using multi seed crystals with controlled configurations, which provide simplification and systematical control of multicrystalline structure.

We found that sub-GBs are generated from grain boundaries and their amount depends on the grain boundary structure. Furthermore, finite element stress analysis modeling the experimented multicrystalline structure revealed that local shear stress around the grain boundary is the key driving force of the sub-GBs generation. This research insist that controlling the grain boundary structure in the practical growth method is a reliable way to suppress the sub-GBs generation.

These fundamental knowledge of sub-GBs should be applicable to improve the material performance of Si multicrystals and promise high efficiency solar cells, although interaction with impurities and vanishing mechanism of sub-GBs remain to be investigated.
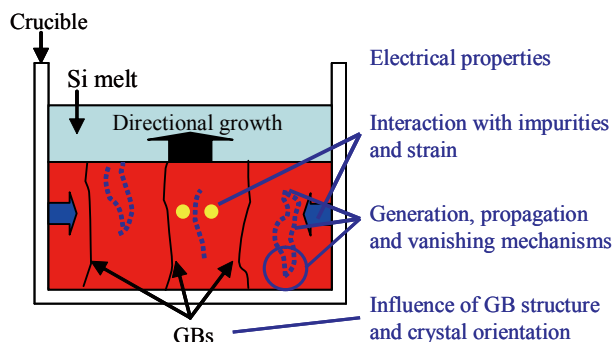
References
[1] K. Fujiwara, W. Pan, N. Usami, K. Sawada, M. Tokairin, Y. Nose, A. Nomura, T. Shishido and K. Nakajima, Acta Mater., **54**, 3191 (2006).
[2] N. Usami, K. Kutsukake, K. Fujiwara, and K. Nakajima, J. Appl. Phys., **102**, 103504 (2007).
[3] K. Kutsukake, N. Usami, K. Fujiwara, Y. Nose, and K. Nakajima, Mater. Trans., **48**, 143 (2007).

Contact to
Kazuo Nakajima (Crystal Physics Division)
e-mail: nakasisc@imr.tohoku.ac.jp

Fig.1. Research topics of sub-GBs in Si bulk multicrystals.

Do Si Single Crystal Balls Save the World from the Global Energy Crisis?

Spherical Si single crystals for solar cell substrates have been grown successfully with a yield of almost 100% by optimizing the supercooling for the recrystallization of Si droplets that were once fabricated by the jet-dropping method.

Among solar cells based on various materials, crystalline Si wafer-based photovoltaic modules, i.e., single- and multi-crystalline-Si solar cells, are running ahead, dominating almost 90% of the world's photovoltaic (PV) production. Although Si whose Clarke number is 25.8 is the second most abundant element in the earth crust, a Si-based solar cell is not an exception that has to be on the track of the cost reduction to expand the market besides aiming at the high conversion efficiency. Spherical Si solar cells attract considerable attention because of the expected feature of low-waste and low cost fabrication. The advantage of spherical Si crystals fabricated using dropping method is that the Si crystals can be fabricated directly from dropping molten Si without any fabrication process that is always required in the production of the Si wafer-based devices. This results in a great potential for low-waste and low cost fabrication of solar cell substrates.

Increasing the energy conversion efficiency to the theoretical value has been a super tough challenge to Si wafer-based PV devices, either single crystalline or multicrystalline. 1 % increment has required bloody efforts of a number of people, a couple of decades and plenty of money. Although the conversion efficiency of spherical Si-based solar cells is approximately 2-3 % lower than that made from Si wafer-based ones, the increment of the efficiency is remarkable these years. This is because we have good understanding of degradation of lifetime associated with crystalline defects [1,2] and we have also found the optimum growth condition in terms of supercooling of a Si droplet for the completely crystalline Si sphere [3].

The recrystallization process of Si droplets was studied. Several hundreds spherical Si multicrystals per second with a diameter of approximately 400 µm in a teardrop shape were initially fabricated by jet-dropping method controlling temperature of the furnace and pressure of atmosphere in the system.

The as-jetted spherical Si multicrystals were then annealed at 1000°C for 2-5 hours in a mixed atmosphere of oxygen and nitrogen to form oxide films (SiO_2) on their surface. Then the spherical Si multicrystals were melted to droplets on a silica plate in an atmosphere of oxygen, and the Si droplets were recrystallized to be single crystals at supercooling of a certain range (Fig. 1). It was found that the recrystallization process occurred unidirectionally in each Si droplet and recrystallized spherical Si single crystals free of defects (dislocations and oxidation induced stacking faults, OSF) was obtained at a supercooling in the range of 12-42°C (Fig. 2). Under this condition, spherical Si single crystals for solar cell substrates have been grown successfully with a yield of almost 100%. While the crystal growth showed a dendritic growth mode and only multicrystals was obtained when the supercooling was larger than 87°C.

References
[1] T. Taishi, T. Hoshikawa, M. Yamatani, K. Shirasawa, X. Huang, S. Uda and K. Hoshikawa, J. Cryst. Growth, **306**, 452 (2007).
[2] T. Hoshikawa, T. Taishi, X. Huang, S. Uda, M. Yamatani, K. Shirasawa and K. Hoshikawa, J. Cryst. Growth, **307**, 466 (2007).
[3] X. Huang, S. Uda, H. Tanabe, N. Kitahara, H. Arimune and K. Hoshikawa, J. Cryst. Growth, **307**, 341 (2007).

Contact to
Satoshi Uda (Crystal Chemistry Division)
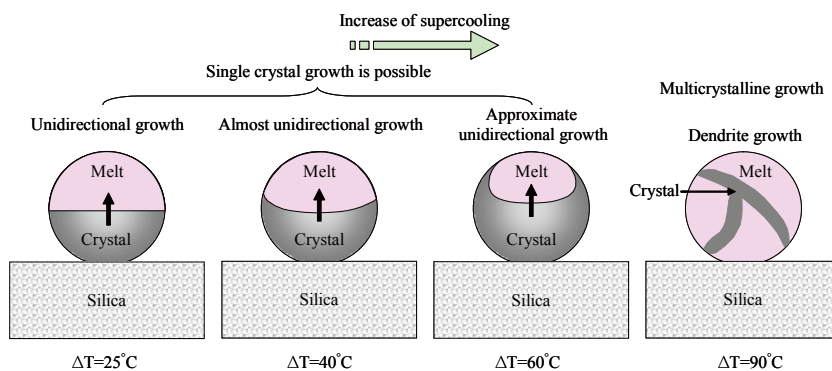e-mail: uda@imr.tohoku.ac.jp

Fig. 1 Recrystallization processes in an isolated Si droplet on a silica plate at different degree of supercooling.
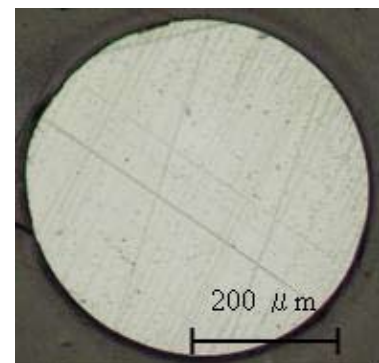

Fig. 2 Cross-section of the recrystallized spherical single Si crystal obtained under the supercooling of 12 ˚C.

Lithium Borohydride: A Light-Weight Hydride Showing "Lithium Super-ionic Conductvity"

The electrical conductivity of lithium borohydride ($LiBH_4$) jumped by three orders of magnitude due to structural transition from orthorhombic to hexagonal phases at approximately 390 K. The hexagonal phase exhibited a high electrical conductivity of the order of 10^{-3} Scm^{-1}. Furthermore, the conductivity obtained from ^7Li-NMR was in good agreement with the measured electrical conductivity. It was concluded that the electrical conductivity in the hexagonal phase is due to the Li super-ionic conduction.

Recently, we have reported that the microwave irradiation process can be applied to the dehydriding (hydrogen release) reaction of $LiBH_4$, a light-weight hydride [1, 2]. The rate of the temperature increase in $LiBH_4$ by the microwave irradiation was drastically enhanced above 380 K, which resulted in a fast dehydriding reaction of $LiBH_4$. At this temperature, $LiBH_4$ undergoes a structural transition from orthorhombic (low temperature (LT)) to hexagonal (high temperature (HT)) phases [3]. From the result of the permittivity (dielectric constants and loss values) measurements, $LiBH_4$ is suggested to be an insulator in the LT phase, while it might be conductive in the HT phase [1]. Therefore, probably due to the conductive loss, the HT phase was rapidly heated. Since hydrogen is covalently stabilized as $[BH_4]^-$, which is then ionically combined with Li^+ [3], it was predicted that the charge carrier is Li^+, and not H^+.

Fig. 1 shows the temperature dependence of the electrical conductivity of $LiBH_4$ [4]. In the heating process, the electrical conductivity increased with increasing temperature. A discontinuous jump was observed at around 390 K, which corresponds to the structural transition temperature. The electrical conductivity of the HT phase was as high as 10^{-3} Scm^{-1}, which is comparable to those of high Li ionic conductors at room temperature. Below and above 390 K, the temperature dependences of the electrical conductivity showed Arrhenius behaviors. The activation energies E_a^σ for the conduction were evaluated to be of 0.69 eV and 0.53 eV for the LT and HT phases, respectively. In the cooling process, the discontinuous jump of the electrical conductivity was observed at a lower temperature. The hysteresis of approximately 10 K was in accordance with that observed by the differential scanning calorimeter curves, as shown in the inset of Fig. 1.

The ^7Li-NMR data showed a fairly good agreement with the measured electrical conductivity [4]. Thus, it can be concluded that the high electrical conductivity of the order of 10^{-3} Scm^{-1} in the HT phase originated from the fast Li ionic motion. Moreover, the calculated electrical conductivity for dimensional factor $n = 4$ showed better agreement with the measured electrical conductivity than that for $n = 6$.

As shown in Fig. 2, the nearest-neighbor of Li arrange along the a and b axes without hindrance at the HT phase [4]. The rearrangement might enable the Li^+ to migrate along each axis.
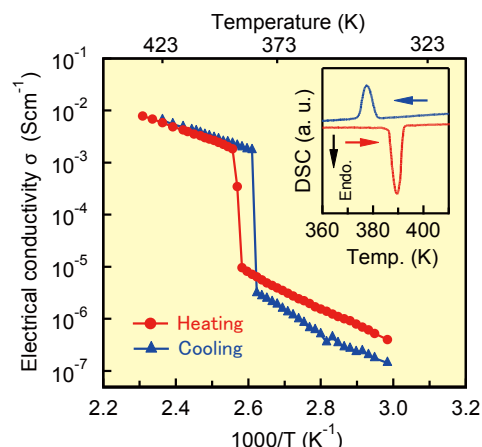

Fig. 1 Temperature dependences of the electrical conductivity of $LiBH_4$. Inset shows the differential scanning calorimeter (DSC) of $LiBH_4$. Red and blue lines correspond to data taken during heating and cooling process, respectively.
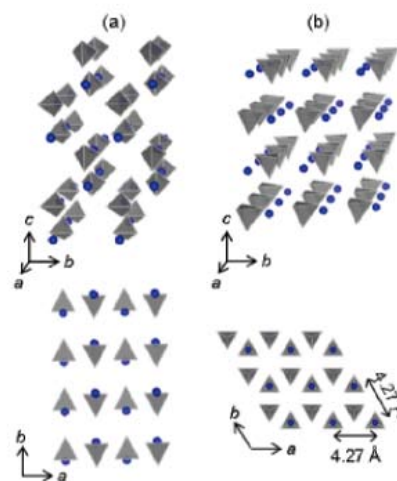

Fig. 2 Crystal structures of $LiBH_4$ in the (a) orthorhombic (low temperature (LT)) and (b) hexagonal (high temperature (HT)) phases. Blue ball and gray tetrahedron show Li and BH_4, respectively.

References

[1] Y. Nakamori, S. Orimo and T. Tsutaoka, *Appl. Phys. Lett.,* **88**, 112104 (2006).

[2] M. Matsuo, Y. Nakamori, K. Yamada and S. Orimo, *Appl. Phys. Lett.,* **90**, 232907 (2007).

[3] S. Orimo, Y. Nakamori, J.R. Eliseo, A. Züttel and C.M. Jensen, *Chem. Rev.,* **107**, 4111 (2007).

[4] M. Matsuo, Y. Nakamori, S. Orimo, H. Maekawa and H. Takamura, *Appl. Phys. Lett.,* **91**, 224103 (2007).

Contact to
Shin-ichi Orimo (High-Temperature Materials Science Division (Environmental Materials Science))
e-mail: orimo@ imr.tohoku.ac.jp

Design of Tetraketone Ligands with Chelate Effect for Active Materials of Uranium Redox- Flow Battery

Depleted uranium, derived as a major by-product of enrichment process of the nuclear fuel, has been deposited and its total weight will exceed two million tons in the world by 2015. Since its conventional use in counterweights, shielding materials, and depleted uranium shell was unsuccessful, efforts have been paid for potential applications to various materials. Whereas none of them has been put to practical use. Taking account of the electrochemical nature of uranium, we have proposed uranium redox-flow battery with potential high energy-efficiency.

We have focused our attention on the inherent nature of light actinides (An) that there are two couples of isostructural ions, namely An^{n+} (n = 3 and 4; n is oxidation number) and $AnO_2^{(n-4)+}$ (n = 5 and 6). Within the couples of the isostructural ions, rapid kinetics of electron transfer (ET) is expected to lower electrochemical overvoltage according to the Butler-Volmer law (Fig. 1). This is clear contrast to the vanadium redox-flow battery presently in operation consisting of aqueous electrolyte (V^{2+}/V^{3+} for negative and VO^{2+}/VO_2^+ for positive electrolytes) which suffers from low energy efficiency due to slow kinetics of the ET especially of VO^{2+}/VO_2^+ couple requiring oxygen transfer.

We have demonstrated neptunium (Np) battery with aqueous electrolytes [1, 2]. Our recent study has focused on the application of uranium (U) as an active material of the redox-flow battery in use of leveling of electric power generated by natural energy such as wind power.

The β-diketonates of uranium are the first candidates for the active materials studied. The metal β-diketonates with chemical functionalities and toughness for light and heat have been applied to electroluminescence (EL) materials and precursors of metallorganic chemical vapor deposition (MOCVD) for oxide materials.
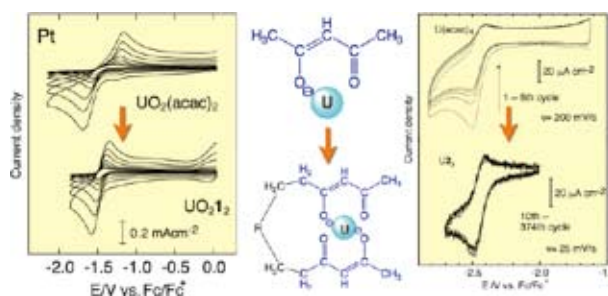
Fig. 2 Dimerization of ligand yields a dramatic improvement of kinetics and thermodynamics as active materials of uranium redox-flow battery.

Cyclic voltammetry of β-diketonates of U(VI)/U(V) and U(IV)/U(III) displays multiple couples of peaks and suggests dissociative ET, *i.e.* ET followed by chemical reaction (EC), due to smaller effective charge carried by the reduced metal center. Assuming enhanced stability of the reduced complex, the electromotive force (EMF) of the single-unit cell of the battery is estimated more than 1.0 V from the difference between $E_{1/2}$ for two-coordinated complexes of U(VI)/U(V) and that for four-coordinated ones of U(IV)/U(III). This value is comparable to 1.2 V of the vanadium battery. One of the reasonable strategies is use of chelate effect by cyclic or multidentate ligands such as crown ethers which form stable complexes even with alkaline metal ions with least complexing ability. In order to stabilize the complexes with U(V) and U(III), we have developed dimerized tetraketone ligands (Fig. 2) [3]. By using the tetraketone the demonstration of the uranium battery was carried out by successful charge and discharge experiments.

References
[1] T. Yamamura, N. Watanabe and Y. Shiokawa, J. Alloys Compds., **408-412C**, 1260 (2006).
[2] T. Yamamura, N. Watanabe, T. Yano and Y. Shiokawa, J. Electrochem. Soc., **152**, A830 (2005).
[3] T. Yamamura, K. Shirasaki, H. Sato, Y. Nakamura, H. Tomiyasu, I. Satoh and Y. Shiokawa, J. Phys. Chem. C, **111**, 18812 (2007).

Contact to
Tomoo Yamamura (Radiochemistry of Metals Division)
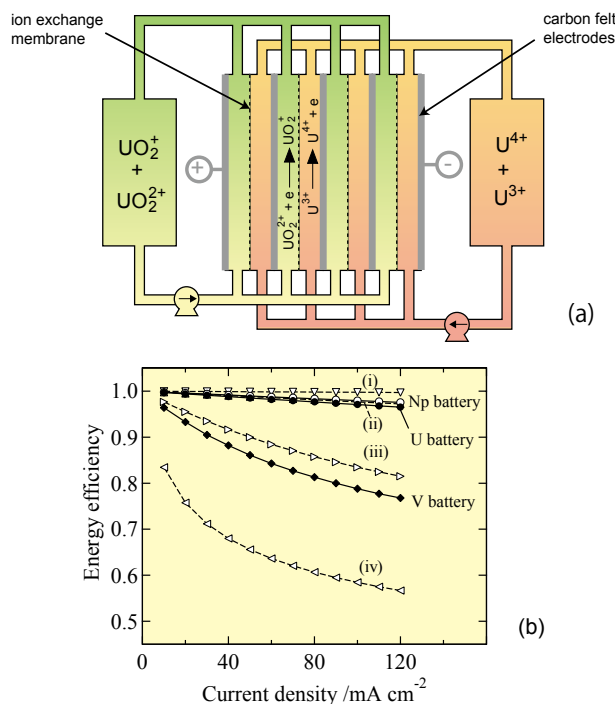e-mail: yamamura@imr.tohoku.ac.jp

Fig. 1. (a) Schematic diagram of uranium redox-flow battery. (b) Comparison of energy efficiency of redox-flow batteries using active materials of neptunium, uranium, and vanadium, and using that of k_0 = 10^{-1} (i), 10^{-2} (ii), 10^{-3} (iii), and 10^{-4} (iv).

Spatially-resolved Observation of Glow Discharge Plasma for Atomic Emission Spectrometry

An imaging spectrograph equipped with a CCD detector was employed to measure two-dimensional emission images from a glow discharge plasma in atomic emission spectrometry. The emission images at Zn I 334.50 nm for a zinc sample could be obtained. Their emission intensities were not uniform in the radial direction of the plasma region but became weaker at larger distance from the central zone. The two-dimensional distribution would result from a spatial variation in the excitation efficiency of the plasma and thus provide useful information for understanding the excitation processes occurring in the plasma.

A two-dimensional (2D) image of the spectrum emitted from the glow discharge plasma would give useful information not only for determining the experimental conditions in the analytical application but for studying the excitation processes occurring in the plasma. This paper indicates 2D images of the emission signal in the radial direction of the glow discharge plasma, when a zinc emission line is observed by using a two-dimensionally imaging spectrometer having a good spectral resolution of less than 1 nm.

Experimental

Figure 1 shows the block diagram of the measuring system employed. A glow discharge lamp was made in our laboratory according to the original model of Grimm, where the inner diameter of the hollow anode was 8.0 mm and the distance between the anode and cathode sample was adjusted to be 0.2-0.4 mm. Emission signals from the glow discharge lamp, which were observed from the axial direction of the plasma, were conducted through a collimator optics onto the entrance slit of an image spectrograph (Model 12580, BunkoKeiki Corp., Japan), and the emission image was then dispersed and detected on a charge-coupled device detector (SensiCam QE Model, PCO Imaging Corp., Germany), where the 2D image of a particular emission line could be observed in the radial direction of the plasma.[1] A 2D image obtained by 5 x 5 pixels corresponded to an actual sample area of 0.1 x 0.1 mm^2. The spectral resolution was 0.1-1.0 nm depending on the slit width. Pulsated discharge voltages were applied to the glow discharge lamp with a high-speed high-voltage amplifier (HEOPT-B60-L1, Matsusada Precision Inc., Japan), which was controlled with a function generator (Model 4502, Kikusui Corp., Japan).The discharge parameters are described later. High-purity argon (>99.999 %) was introduced as the plasma gas after evacuating the chamber to below 10 Pa. The pressure was monitored with a Pirani gauge (GP-2, ULVAC Corp., Japan), which had been corrected for pure argon, which were placed between the evacuation port and a
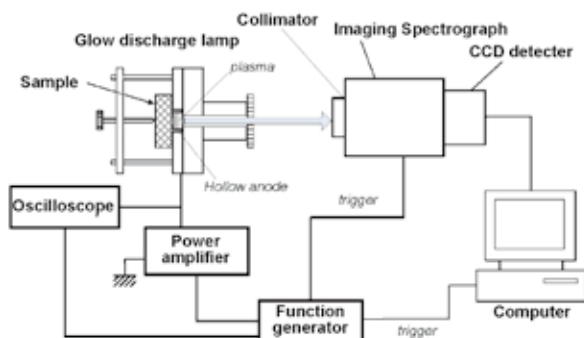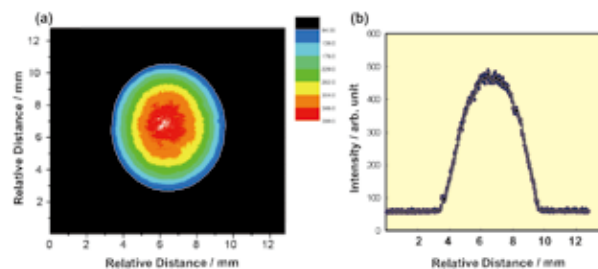

Fig. 1 Block diagram of the measuring system.

Fig. 2 Two-dimensional emission image of the Zn I 334.50-nm line observed from the axial direction of a glow discharge plasma (a) and the cross-section distribution of the emission intensity along the radial distance (b).

rotary vacuum pump (GLD-166, ULVAC Engineering Inc., Japan). The plasma gas was flowed during the measurement on keeping a chamber pressure of 5.3 x 10^2 Pa.

Results and Discussion

Figure 2 shows a 2D emission image (a) for the zinc sample, whose intensities are expressed by mapping with several colors, and the cross-section distribution (b) along the radial distance of the plasma.[2] The analytical lines was Zn I 334.50 nm (7.78 eV). For this measurement, a pulsated discharge mode was employed, where the frequency of the discharge was 100 Hz, the duty ratio was 10 %, the maximum voltage was 450 V, and the minimum voltage (offset voltage) was 50 V. The pulsated discharge is required to accumulate the emission image in the CCD detector, and it is also useful to control the sputtering rate appropriately. The slit width of the spectrometer was 2.0 mm and the gate width of the CCD detector was 1 ms. The emission signal was stored in the CCD detector during 32 discharge pulses, and this accumulation was 100-times replicated and averaged on the personal computer. Note that the diameter of the hollow cathode is 8.0 mm; therefore, this diameter restricts the plasma zone. It can be clearly demonstrated that the emission of the samples is not irradiated uniformly over the possible plasma zone but has a large variation in the intensities along the radial distance. The central portion having a diameter of about 2 mm gives the most intense emission. The concentric-circles pattern means that the emission intensity becomes weaker with increasing the diameter. This effect is probably because plasma parameters determining the excitation processes, such as electron density and electron temperature, might be changed in the radial direction of the glow discharge plasma. We are not surprised at this result, because the plasma region should reach a boundary near the hollow anode (anode dark space) and the resulting emission is thus extinguished. However, the shape of the emission zone and the intensity distribution have not been reported in previous papers. This result could provide novel information for understanding the excitations occurring in the glow discharge plasma.

References
[1] C. Kitaoka and K. Wagatsuma: Anal. Sci., **23**, 1261 (2007).
[2] Y. Zenitani and K. Wagatsuma: Anal. Sci., **24**, 555 (2008).

Contacted to
Kazuaki Wagatsuma (Analytical Science Division)
e-mail: wagatuma@imr.tohoku.ac.jp

20 T Superconducting Outsert Magnet with a 400 mm Room Temperature Bore for a 45 T Hybrid Magnet

To construct a high field magnet with compact and energy-saving design as well as with easy operation and maintenance, we have been developing high-strength Nb_3Sn strand cables, with maximized superconducting characteristics and which can withstand a large electromagnetic force over 500 MPa. A 20 T superconducting magnet with a room temperature bore ($\Phi=400$ mm) consisting of five layers made of $CuNb/Nb_3Sn$ and two layers of NbTi was designed. The 20 T superconducting coil will be used as a 20 T outsert to obtain a 45 T hybrid magnet.

The magnetic field is one of the most important thermodynamical parameters to study physical properties of the materials and the physical effects in general. Our aim is to fabricate a compact and energy-saving laboratory hybrid magnet with easy operation and maintenance. To succeed it is necessary to develop high-strength Nb_3Sn strand cables with high critical currents and good enough mechanical properties to withstand a large electromagnetic force over 500 MPa. We have recently shown that the critical current greatly enhances when as-reacted Nb_3Sn strands are repeatedly bent at room temperature (prebending treatment) [1]. This critical current enhancement effect of $CuNb/Nb_3Sn$ strands is related to improvement of the upper critical field and of the transition temperature due to relaxation of the thermal residual strain [2].

In order to investigate the application of the prebending effect to strand cabling process, two kinds of strand cables were fabricated by cabling the reacted $CuNb/Nb_3Sn$ strands. Strands and cables were produced by the Furukawa Electric Company. We intended to develop the 3+4 strand cable consisting of three $CuNb/Nb_3Sn$ strands and four stainless steel strands. The 3 strand cable composed of three $CuNb/Nb_3Sn$ strands was also prepared for comparison. Fig. 1 shows the schematic cross sectional view of the designed $CuNb/Nb_3Sn$ strand cables. To ensure an operation current of 1000 A for the designed $CuNb/Nb_3Sn$ strand cables, the diameter of a $CuNb/Nb_3Sn$ strand was determined as a function of magnetic field. The operation temperature was selected to be 2.0 K of the superfluid helium condition and it is the temperature of the operation current margin.

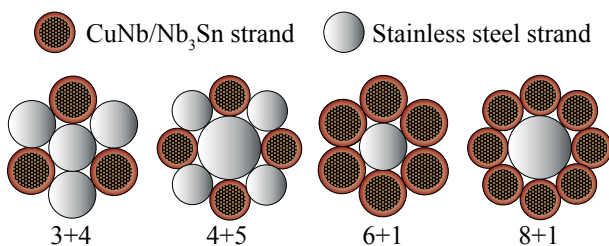The designed outsert will come across the full excitation current of 1,000 A at 22 T, and the current margin up to 1,000 A will lead to the coil operation stability. The magnetic stored energy is estimated to be 144 MJ at 20 T. Fig. 2 shows the magnetic field generation at the coil equator. The maximum hoop stress appears in the outer layer $CuNb/Nb_3Sn$ section coils, and the hoop stress value of around 480 MPa is supposed. The maximum compressive stress is calculated to be 81 MPa for the $CuNb/Nb_3Sn$ layer coil and 127 MPa for the NbTi layer coil. The coil space current density is 22.1 A/mm^2 as low as 62% of the conductor current density for the innermost layer coil. We found that the 20 T-Φ400 mm RT-bore superconducting outsert can be reasonably designed as compactly as possible.
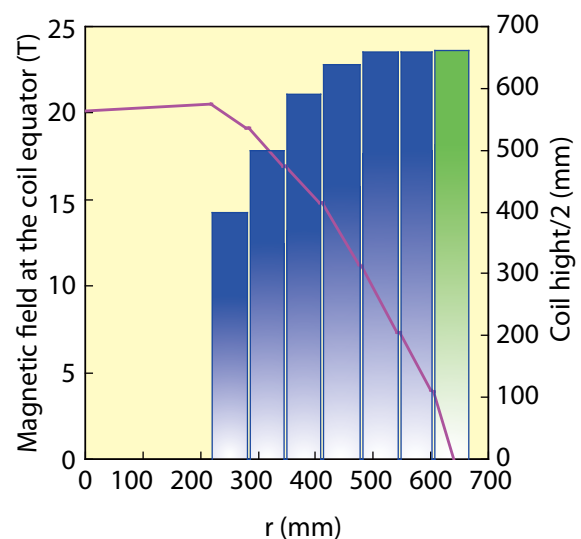

Fig. 2. Magnetic fields generated at the coil equator for a 20T-Φ400 mm room temperature bore superconducting outsert. The layers with blue and green colors are Nb_3Sn and NbTi coils, respectively. The generated magnetic field is 20 T at the center of the coil. The maximum coil height is 1321 mm at the L7 NbTi layer coil.

References
[1] K. Watanabe, S. Awaji, H. Oguro, G. Nishijima, K. Miyoshi, and S. Meguro, IEEE Trans. Appl. Supercond., **15**, 3564 (2005).
[2] H. Oguro, S. Awaji, G. Nishijima, P. Badica, K. Watanabe, F. Shikanai, T. Kamiyama, and K. Katagiri, J. Appl. Phys., **101**, 103913 (2007).

Contact to
Kazuo Watanabe (High Field Laboratory for Superconducting Materials)
e-mail: kwata@imr.tohoku.ac.jp

Fig. 1. Schematic cross section of high strength strand cables composed of $CuNb/Nb_3Sn$ strands and stainless steel strands.

Ab initio Study of Single-molecule Rotation Switch Based on Nonequilibrium Green's Function Theory

Molecular electronics is expected to be realized after the ending of silicon technology in 10 years, where the first principles based calculations play important role, since up to the present there have been difficulty to explore experimentally the switching properties in nanoscale. The present work showed an interesting behavior of single-molecular switch, which is based on the rotation of the molecule. The method used in the paper is based on the nonequilibrium Green's function and the code has been developed originally in our research group. All the numerical calculations have been conducted by using the HITACHI SR11000 supercomputer at the Center for Computational Materials Science, IMR.

The bistable molecular switches have been studied theoretically based on the first-principles calculation. The geometry structures of the switches studied here can be triggered between two symmetrical structures by using an external applied electric field. *I-V* characteristic curves of the different molecule configurations have been calculated, and distinguishability of these characteristic curves indicates a switching behavior, the performance of which can be improved significantly by selecting suitable donors and acceptors [1].

Figure 1 shows the presently estimated potential energy surface of the isolated molecule as a function of dihedral without bias voltage. The arrows indicate the bistable structures. We define the left state as 1 and the right one as 0 for one bit of future computing unit. The inset shows geometries of two states.
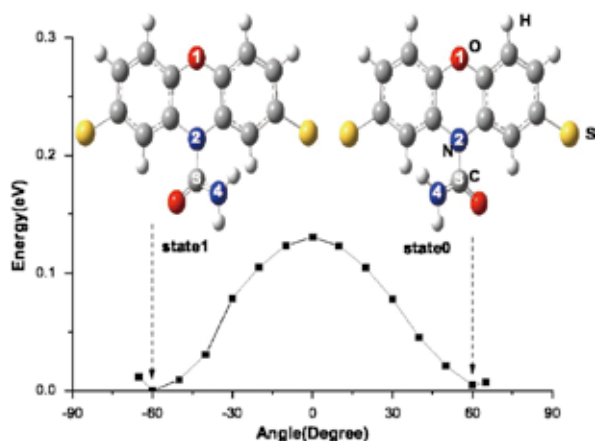

Fig.1. Example of single-molecular rotation switch for molecular device.

Figure 2 gives Au-lead/molecule/Au-lead open system and its energy level diagram with bias which drives the system out of equilibrium. μ_1 (μ_2) represents the quasi-Fermi level of the left (right) Au lead. The direction of bias is from right to left shown in Fig. 2, with (μ_1) greater than (μ_2). If one energy level lies between two quasi-Fermi levels (see Fig. 2 (2)) , the left lead would like to see more electrons occupying this level and keep charging them in, while the right one

would like to see fewer electrons and keep pulling them out, or equivalently, more holes pump into this level from the right lead. In this case, the energy level acts as a channel, and the current flows through this channel.
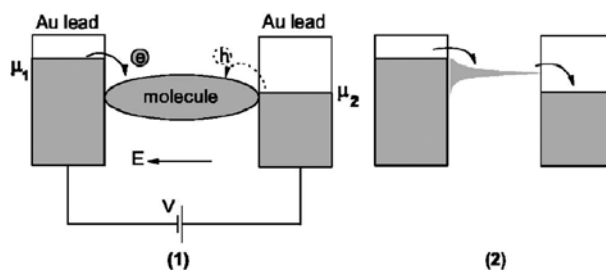

Fig. 2. Au-lead/molecule/Au-lead open system (1) and its energy level diagram (2).

The calculated *I-V* characteristics for the two structures are presented in Fig. 3. The current curves of two states can be distinguished, indicating switching behavior. The current through state 1 is significantly higher than the current through state 0, and the maximum current ratio of the two states is about 5. This suggests that the switching performance is acceptable for real applications.
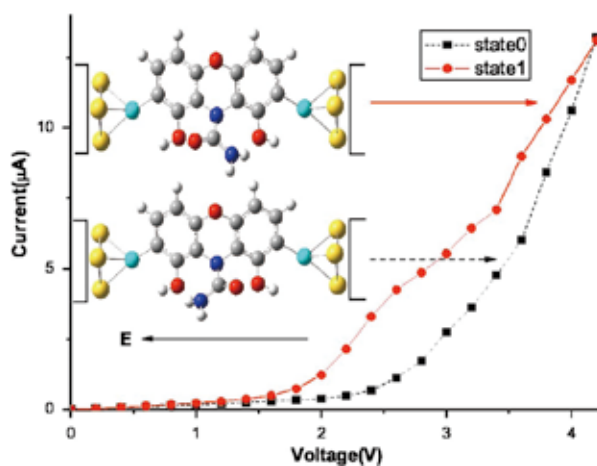

Fig.3. *I-V* characteristics for donor –OH, and their geometries of two states and the direction of the applied field are depicted in inset.

Reference

[1] Y. Y. Liang, F. Jiang, Y. X. Zhou, H. Chen, R. Note, H. Mizuseki, and Y. Kawazoe, J. Chem. Phys. **127**, 084107 (2007).

Contact to
Yoshiyuki Kawazoe (Materials Design by Computer Simulation Division)
e-mail: kawazoe@imr.edu